

Detecting induced polarisation effects in time-domain data: a modelling study using stretched exponentials

Seogi Kang, Douglas W. Oldenburg & Lindsey J. Heagy

To cite this article: Seogi Kang, Douglas W. Oldenburg & Lindsey J. Heagy (2020) Detecting induced polarisation effects in time-domain data: a modelling study using stretched exponentials, Exploration Geophysics, 51:1, 122-133, DOI: [10.1080/08123985.2019.1690393](https://doi.org/10.1080/08123985.2019.1690393)

To link to this article: <https://doi.org/10.1080/08123985.2019.1690393>



Published online: 27 Nov 2019.



Submit your article to this journal



Article views: 273



View related articles



View Crossmark data



Citing articles: 5 View citing articles



Detecting induced polarisation effects in time-domain data: a modelling study using stretched exponentials

Seogi Kang , Douglas W. Oldenburg  and Lindsey J. Heagy 

Geophysical Inversion Facility, University of British Columbia, Vancouver, BC, Canada

ABSTRACT

The potential for extracting and interpreting induced polarisation (IP) data from airborne surveys is now broadly recognised. There is, however, still considerable discussion about the conditions under which the technique can provide knowledge about the subsurface and thus, its practical applications. Foremost among these is whether, or under what conditions, airborne IP can detect chargeable bodies at depth. To investigate, we focus on data obtained from a coincident-loop time-domain system. Our analysis is expedited by using a stretched exponential rather than a Cole-Cole model to represent the IP phenomenon. Our paper begins with an example that illuminates the physical understanding about how negative transients (the typical signature of an IP signal in airborne data) can be generated. The effects of the background conductivity are investigated; this study shows that a moderately conductive and chargeable target in a resistive host is an ideal scenario for generating strong IP signals. We then examine the important topic of estimating the maximum depth of the chargeable target that can generate negative transients. Lastly, some common chargeable earth-materials are discussed and their typical IP time-domain features are analysed. The results presented in this paper can be reproduced and further explored by accessing the provided Jupyter notebooks.

ARTICLE HISTORY

Received 1 October 2018
Accepted 10 September 2019

KEY WORDS

Airborne electromagnetics;
induced polarisation;
electromagnetic geophysics

1. Introduction

Some earth materials are chargeable because they can store charge when an electric field is applied by an electromagnetic (EM) source. This is often called the induced polarisation (IP) phenomenon. These materials can have different polarisation mechanisms which results in different IP characteristics as a function of frequency. This can be translated into a complex conductivity model such as the Cole-Cole conductivity model (Cole and Cole 1941; Pelton et al. 1978; Tarasov and Titov 2013):

$$\sigma_{cc}(\omega) = \sigma_\infty - \frac{\eta_{cc}\sigma_\infty}{1 + (\omega\tau_{cc})^{c_{cc}}}, \quad (1)$$

where σ_∞ is the conductivity at infinite frequency, η_{cc} is the chargeability, τ_{cc} is the time constant (s), and c_{cc} is the frequency exponent; the subscript CC indicates Cole-Cole.

IP surveys have been successfully conducted in a variety of geoscience applications. For mining, IP surveys are recognised as a principal geophysical technique for finding disseminated sulphides or porphyry deposits (Fink et al. 1990). Non-metallic materials such as clays and ice can also generate IP signals (Grimm and Stillman 2015; Leroy and Revil 2009); this makes IP a useful technique in a range of environmental applications. Grounded DC-IP surveys have been successfully used

for both mining and environmental applications for the past decades. Airborne EM (AEM) systems can also detect IP signals. In particular time-domain AEM surveys using a coincident-loop system sometimes display a negative transient; this is a distinctive IP signature (Weidelt 1982). Compared to EM signals, these negatives (IP signals) are much smaller in amplitude. Hence, for the initial AEM systems, it was not clear if the measured negatives were signals from chargeable materials or if they were simply noise generated by power lines or electric fences (Smith and Klein 1996). With time however, instruments have improved and the validity of negative transients as signal has been firmly established (Macnae 2016; Viezzoli, Kaminski, and Fiandaca 2017). For instance, consistent negatives were recorded over the Tli Kwi Cho kimberlite deposit with three different AEM systems (Kang, Fournier, and Oldenburg 2017). As the quality of instrumentation improves, it is expected that more IP signals will be measured in airborne data. This ability provides motivation for developing methodologies that can extract chargeability information from airborne IP data. Various approaches, including simple curve-fitting, 1D inversions, and 3D inversions have been developed and successfully applied to field examples (Hodges and Chen 2014; Kaminski and Viezzoli 2017; Kang and Oldenburg 2017; Kratzer and Macnae 2012; Kwan et al. 2015). There is a significant

enthusiasm for the potential use of the airborne IP techniques in a variety of applications (e.g. mining and groundwater). However, setting proper expectations about the technique, and recognising its limitation based upon the physics and the current system specifications, is crucial because neither overselling nor underselling the technique is beneficial for the community.

Macnae (2016) investigated the physics of airborne IP and its practical aspects using a simple thin-sheet solution. A main conclusion from his study was that airborne IP is effectively a surficial clay mapper ($z < 100$ m). Viezzoli, Kaminski, and Fiandaca (2017), showed the potential that a deeper chargeable target, such as a mineral deposit ($z > 100$ m), can be detected. That work however, was based upon analysis using 1D simulations. Hence, there is disagreement about the potential depth of investigation of the airborne IP technique. Although the approximate thin-sheet solution and semi-analytic 1D solutions used in Macnae (2016) and Viezzoli, Kaminski, and Fiandaca (2017), respectively, can illustrate some meaningful concepts with respect to airborne IP, these approaches are limited in their ability to model the physics in the presence of complex conductivity structures. For instance, the finite size of the chargeable structure (e.g. width and length) is not taken into account in either approach. Investigating the feasibility of airborne IP in realistic geologic settings requires the use of 3D numerical simulations that solve the full Maxwell's equations.

In this paper, we first develop a convolutional time-domain EM (TEM) simulation code using a stretched exponential (SE) conductivity function (Kohlrausch 1854). We then use this code to investigate four main questions related to the feasibility of the airborne IP under ranges of circumstances:

- How does chargeable material in the subsurface generate negative transients in coincident-loop systems?
- How does the background conductivity affect the IP signals?
- To what depth can we expect to detect a chargeable body?
- What are the characteristics of detectable chargeable materials in AEM data?

For our feasibility study, we limit our attention to detectability of IP signals, and we do not address issues of resolvability of chargeable structures in the inversion; that issue is beyond the scope of this study.

2. Simulating airborne IP data using a stretched exponential

With a complex conductivity, $\sigma(\omega)$, the current density, \vec{j} , in the frequency domain, can be written as:

$$\vec{j} = \sigma(\omega)\vec{E}, \quad (2)$$

where \vec{E} is the electric field (V/m). In the time-domain, the current density, \vec{j} , is:

$$\vec{j} = \sigma(t) \otimes \vec{e}, \quad (3)$$

where \otimes is a convolution. Then Maxwell's equations can be written as

$$\vec{\nabla} \times \vec{e} = -\frac{\partial \vec{b}}{\partial t} \quad (4)$$

$$\vec{\nabla} \times \mu^{-1}\vec{b} - \vec{j} = \vec{j}_s, \quad (5)$$

where \vec{b} is the magnetic flux density (Wb/m²) and \vec{j}_s (A/m²) is the current source; μ is the magnetic permeability (H/m). By discretising and solving the above equations in 3D, we can compute TEM data that include IP effects (Marchant 2015; Marchant, Haber, and Oldenburg 2014). For the discretisation of Equations (2)–(5), an open-source geophysical simulation and inversion package, SimPEG, is used (Cockett et al. 2015). The developed SIMPEG-EMIP code works for both 3D tensor meshes and 2D/3D cylindrical meshes (Heagy et al. 2017). Although not shown in the paper, the SIMPEG-EMIP code can handle arbitrary waveforms such that user can input actual system waveforms used for their own case studies. For further details about solving the convolutional form of Maxwell's equations, see Appendix 1. The code is tested with an analytic solution described in Appendix A.2.

For a time-dependent conductivity, $\sigma(t)$, we use the stretched exponential (SE) model rather than the Cole-Cole model defined in the frequency-domain (Equation (1)). The SE conductivity for a step-off function, $1 - u_{step}(t)$, can be written as

$$\begin{aligned} \sigma_{se} \otimes (1 - u_{step}) &= \sigma_0 \left(1 - u_{step}(t) \right) \\ &\quad - \sigma_\infty \eta_{se} \exp \left(- \left(\frac{t}{\tau_{se}} \right)^{c_{se}} \right) u_{step}(t), \end{aligned} \quad (6)$$

where $u_{step}(t)$ is the Heaviside step function, $\sigma_0 = \sigma_\infty(1 - \eta_{se})$ is the DC conductivity, and subscript SE stands for stretched exponential. We want to obtain σ_{se} from Equation (6). Taking the derivative with respect to time and multiplying by -1 yields:

$$-\frac{\partial}{\partial t} (\sigma_{se} \otimes (1 - u_{step})) = \sigma_{se}(t) \otimes \delta(t) = \sigma_{se}(t), \quad (7)$$

where $\delta(t)$ is the Dirac-Delta function. Evaluating Equation (7) with Equation (6) results in

$$\begin{aligned} \sigma_{se}(t) &= \sigma_\infty \delta(t) - \sigma_\infty \eta_{se} t^{-1} \left(\frac{t}{\tau_{se}} \right)^{c_{se}} \\ &\quad \times \exp \left(- \left(\frac{t}{\tau_{se}} \right)^{c_{se}} \right) u_{step}(t), \end{aligned} \quad (8)$$

A main reason why we used the SE conductivity function rather than the Cole-Cole function is its numerical

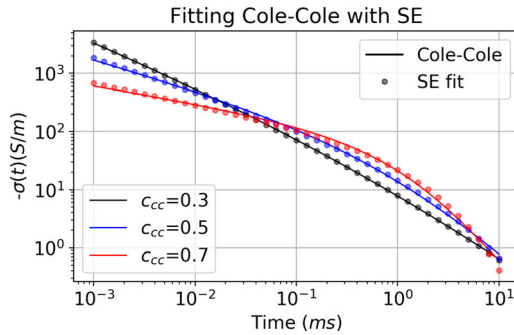


Figure 1. The stretched exponential (SE) fit of the Cole-Cole conductivity in the time domain. Solid lines are the impulse response using a Cole-Cole representation and the circles denote the SE response. At 10^{-3} s, top, middle, bottom curves correspondingly indicate when c_{cc} is 0.3, 0.5, and 0.7.

advantage in the convolutional algorithm. With the SE conductivity, we do not need to convert $\sigma(\omega)$ within each discretised voxel to $\sigma(t)$ because the SE conductivity has an explicit form in the time domain. The SE conductivity will not be beneficial when Maxwell's equations are solved in frequency-domain, and we believe that is the reason why the SE conductivity has not been used extensively, except for the latest simulation study from Belliveau and Haber (2018).

Although the SE conductivity is not exactly the same as the Cole-Cole conductivity (Equation (1)), their time-features are very similar, and when $c_{cc} = 1$ (Debye model), they are equivalent. To illustrate cases when c_{cc} is not equal to 1, we fit the Cole-Cole conductivity with the SE conductivity in time-domain; here, we update all three SE parameters: η_{se} , τ_{se} , c_{se} to fit Cole-Cole conductivity. Figure 1 shows example Cole-Cole conductivity decays ($t > 0$) with variable c_{cc} , and their fits with the SE conductivity. For the range of times of interest (10^{-3} – 10^1 ms), the SE function effectively fits the Cole-Cole, as shown in Figure 1. They are essentially coincident. The estimated values of η_{se} and c_{se} are slightly smaller than their respective Cole-Cole counterparts; τ_{se} is coincident with τ_{cc} except when $c_{cc} = 0.2$ (Table 1). Therefore, when interpreting the SE parameters, readers can use their understanding of Cole-Cole parameters and treat the SE and CC parameters as being similar. Note that we have used the impulse response of the Cole-Cole and SE functions when generating the fits. There is no loss of generality in doing this since the response due to an arbitrary waveform can be represented as a linear combination of impulse responses.

3. Numerical experiments

To answer the four questions posed previously, we carry out TEM simulations using the SimPEG-EMIP code. For the spatial discretisation, we use the 2D cylindrically symmetric mesh because of the cylindrical symmetry in the time-domain AEM system, which uses a horizontal loop (See Figure 2). Rather than using a waveform

Table 1. Comparison of the Cole-Cole (CC) and the resultant Stretched Exponential (SE) parameters for variable c_{cc} .

	CC	SE	CC	SE	CC	SE
η_{cc}	0.1	0.09	0.1	0.09	0.1	0.09
τ_{cc} (ms)	1	0.8	1	1	1	1
c_{cc}	0.3	0.2	0.5	0.4	0.7	0.6

Note: The chargeability, timeconstant, and the frequency component are correspondingly represented as η , τ , c ; subscripts CC and SE denote the Cole-Cole and SE parameters.

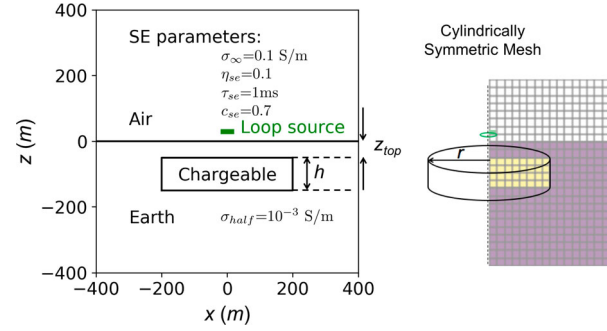


Figure 2. A chargeable cylinder embedded in a halfspace earth. The 13 m-radius source loop is located 30 m above the surface. The depth to the top of the prism is denoted by z_{top} . Right: the 2D cylindrically symmetric mesh is used for TEM simulations.

for a specific AEM system, we use a step-off waveform as an input current. Again, there is no loss of generality since the response from an arbitrary waveform can be generated by a linear combination of step-off responses (Fitterman and Anderson 1987). A horizontal receiver loop measuring the voltage (equivalent to $-db_z/dt$) is coincident with the source loop. A chargeable cylinder is embedded in the resistive halfspace ($\sigma_{half} = 10^{-3}$ S/m). The depth to the top (z_{top}), radius (r), and thickness (h) of the chargeable cylinder are correspondingly $z_{top} = 50$ m, $r = 200$ m, and $h = 100$ m; the SE parameters of the cylinder are $\sigma_\infty = 0.1$ S/m, $\eta_{se} = 0.1$, $\tau_{se} = 1$ ms, $c_{se} = 0.7$; the cylinder is 100 times more conductive than the halfspace and its effective conductance (σh) is 10 S.

To understand how negative transients are caused by the presence of chargeable rocks, we first explore how the electric field diffuses into the earth after the input current is turned off. Figure 3(a) shows the simulated electric field in y -direction (into the page) at four different time channels (0.01–50 ms). At early times (0.01–0.3 ms) electric fields, which rotate in the horizontal plane in a counter-clockwise direction, are induced in both the halfspace and in the conductive cylinder. As time passes, the electric field diffuses downwards and radially outwards; particularly large rotating electric fields are induced in the conductor. These inductive currents are responsible for “charging up” the earth material. At a later time (6 ms), the inductive currents have gone and only the decaying polarisation currents remain. The resultant electric fields (and currents) have

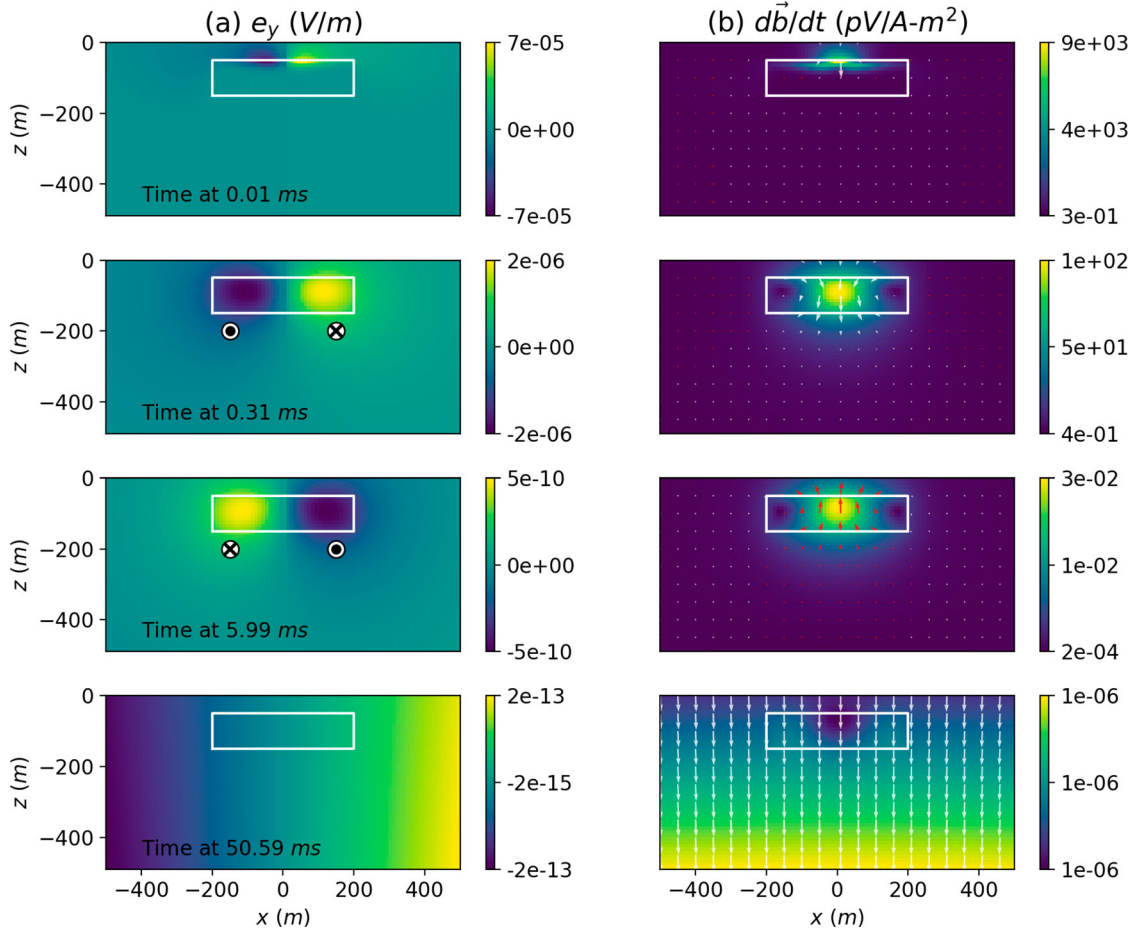


Figure 3. EM fields diffusing in the earth: (a) electric field in y -direction and (b) time derivative of the magnetic field (\vec{db}/dt); the chargeable cylinder is outlined in white. At early times (0.01–0.3 ms), EM induction is dominant; this results in inductive electric fields rotating counter-clockwise and \vec{db}/dt fields going upward. However, at 6 ms the direction of the electric field is reversed (clockwise) as a result of the chargeable cylinder; similarly \vec{db}/dt fields go upward; This results in negative transients at the receiver loop (See Figure 4).

reversed direction; this is due to IP effects. At a later time (50 ms), these IP effects have decayed away. With Faraday's law, electric fields are generated by time-varying magnetic field (\vec{db}/dt), and the measured voltage is the same as the vertical component of $-\vec{db}/dt$. Similarly, Figure 3(b) shows the vectoral distribution of \vec{db}/dt in time. At 0.3 ms, the high amplitude of \vec{db}/dt is shown in the target, and the main direction of \vec{db}/dt (white arrow) is downward. However, at 6 ms the upward direction of \vec{db}/dt (red arrows) is generated by IP effects; this will result in negative transients at the receiver loop. It is important to notice that electric fields generated either from EM or IP effects (Figure 3(a)) do not cross a boundary. There is no charge build up on the boundary and there are no channelled currents (which is the mechanism by which IP signals for the grounded DC-IP surveys are generated). The current channelling could happen if the cylindrical symmetry is broken (e.g. the source loop is located away from the centre of the chargeable cylinder), but our analysis is focused on when cylindrical symmetry is preserved; the IP effects we show are solely due to the inductive polarised currents.

Based upon the physical understanding of IP effects due to a loop source, we examine the data measured at the receiver loop. The black lines in Figure 4(a) show the measured time decays, d^{obs} , (on a log-log scale); negative values are shown after 2 ms (black dashed line). Another simulation is carried out without IP effects ($\eta_{se} = 0$), and the computed data are shown with the blue line (no negatives); we call these the fundamental data, d^F ; they include only EM induction effects. The IP data, d^{IP} , are defined as

$$d^{IP} = d^{obs} - d^F. \quad (9)$$

The system noise-level is set to 10^{-4} pV/A-m² based upon a field data set measured at Mt. Milligan with a VTEM system (Figure 4.23 in Kang (2018)), which denoted as the grey shaded region in Figure 4(a). At the early times ($t < 1$ ms), d^{obs} and d^F are almost coincident indicating that EM induction dominates the response. On the other hand, IP effects are dominant at later times ($t > 2$ ms). To show the relative strength of the IP effects, we define the ratio, R , between $|d^F|$ and $|d^{IP}|$:

$$R = \frac{|d^{IP}|}{|d^F|}. \quad (10)$$

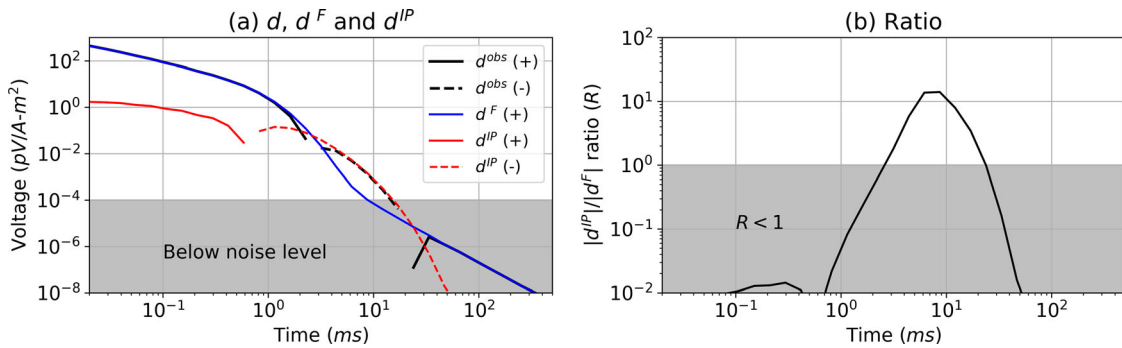


Figure 4. (a) Simulated TEM responses; d^{obs} (black) are observations (EM+IP), d^F (blue) are fundamental (EM) data, and d^{IP} (red) are IP data. Solid and dashed lines distinguish positive and negative values. Signals beneath the noise level ($10^{-4} \text{ pV}/\text{A}\cdot\text{m}^2$) are shown within the grey zone. (b) $R = |d^{\text{IP}}|/|d^F|$ shows the relative strength of the IP signals compared to the fundamental induction effects. In the grey region $R < 1$ and the strength of the IP signal is smaller than the EM signal.

We show R in Figure 4(b); ratios smaller than 10^{-2} are ignored. Between 1 ms and 40 ms R is greater than 0.1, indicating that there are considerable IP effects in the observations. When $R = 1$, the observation is zero which corresponds to the time that the sign reversal occurs.

The EM induction processes within the background conductivity structure influence the electric field, which serves as a forcing function for IP effects. These IP effects translate into the reversed direction of the electric field in the target which results in negative transients that are observed after the EM induction effects have decayed. In the following sections, we carry out TEM-IP simulations to systematically investigate the feasibility of the airborne IP technique. Variable model parameters are shown in Figure 2. Considering the typical AEM system specifications, we limit our attention to the measured time range from 10^{-2} ms to 10^1 ms and to voltages greater than the noise level ($10^{-4} \text{ pV}/\text{A}\cdot\text{m}^2$). Further, for the metric pertaining to whether we can see IP signals or not, we use the existence of the negative datum being greater than the noise floor in the measured time range. Namely, we ignore subtle IP signals smaller than EM signals ($R < 1$).

3.1. Effects of background conductivity on IP signals

As we demonstrated in Figure 3, the electric fields are the forcing functions which generate IP signals. Understanding the effects of the background conductivity on these electric fields is therefore crucial for understanding the resultant IP signals. To investigate this, we perform TEM-IP simulations for a range of values of σ_∞ and σ_{half} . Other parameters for the simulation setup are the same as those in Figure 1 ($r = 200$ m, $h = 100$ m, $z_{\text{top}} = 50$ m, $\eta_{\text{se}} = 0.1$, $\tau_{\text{se}} = 1$ ms, $c_{\text{se}} = 0.7$).

The first experiment involves varying σ_∞ , which ranges from 10^{-4} S/m to 1 S/m, while σ_{half} is fixed to 10^{-3} S/m. Figures 5(a, b) show the simulated time decays and corresponding ratios, R . Negative transients

are only visible when σ_∞ is 0.01 S/m and 0.1 S/m (red and green curves). When σ_∞ is too high (e.g. 1 S/m), EM effects dominate at all times and no negative transients are visible in the observed data. At the other end of the spectrum, the very resistive target shows the smallest R . These results show that a moderately conductive target provides the best opportunity for observing negative transients in the data. When $\sigma_\infty = 1$ S/m, there are no negatives in the time decay curve.

To explore the effect of the halfspace conductivity, σ_{half} , we fix the ratio $\sigma_\infty/\sigma_{\text{half}}$ to be 10, and change σ_{half} from 0.1 S/m to 10^{-4} S/m. In Figure 6, negatives are present when σ_{half} is 10^{-4} S/m and 10^{-3} S/m, but not for the other cases. This shows that when the conductivity of the non-chargeable halfspace is too high (>0.1 S/m), measuring IP signals will be challenging even though chargeable materials exist. Therefore, a moderately conductive target ($\sim 0.01\text{--}0.1$ S/m) in a resistive host ($\sim 10^{-4}\text{--}10^{-3}$ S/m) provides the best circumstances for observing strong IP signals.

3.2. To what depth can we expect to detect chargeable material with airborne IP?

Often, the maximum depth that airborne IP can see chargeable targets is considered to be fairly low ($z < \sim 100$ m from Macnae 2016). However, the possibility exists to see deeper when the host is resistive and the chargeable target is moderately conductive. Here we explore detectability of a chargeable target by altering the depth of the target (z_{top}) from 0 m to 350 m. Figure 7 shows the time decays with variable z_{top} when σ_∞ and σ_{half} are 0.1 S/m and 10^{-3} S/m respectively. Negatives are present when $z_{\text{top}} \leq 200$ m. By decreasing σ_{half} , this depth can be increased to 300 m as shown in Figure 8. Hence, it is possible to detect a deeper chargeable target using the airborne IP technique when the target is moderately conductive and the host rock is resistive (10^{-4} S/m). For instance, at the Tli Kwi Cho kimberlite deposit, negatives were measured near a kimberlite pipe. This moderately conductive pipe was embedded

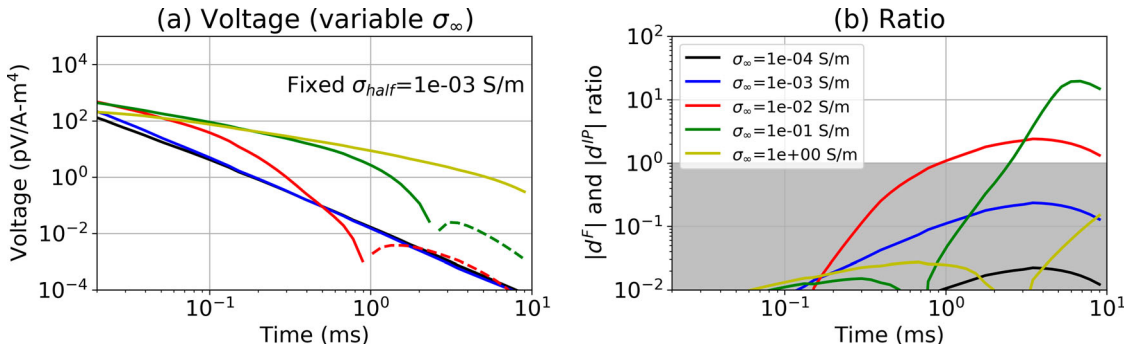


Figure 5. (a) Time decay curves with a variable conductivity of the chargeable cylinder. Solid and dashed lines distinguish positive and negative values. The halfspace conductivity is fixed at 10 $^{-3}$ S/m, whereas σ_∞ varies (10 $^{-4}$ –0.1 S/m). (b) Plots of $R = |d^{IP}|/|d^F|$. In the grey region $R < 1$ and the strength of the IP signal is smaller than the EM signal. The legend for both plots is shown in (b).

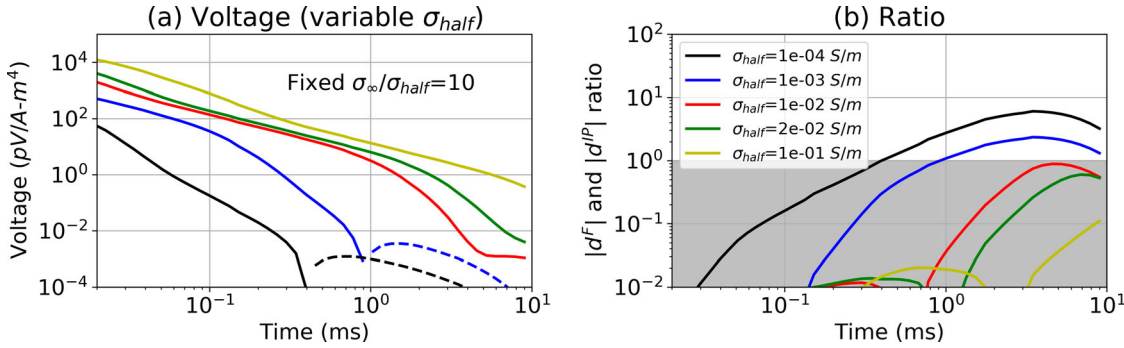


Figure 6. (a) Time decay curves with a variable conductivity of the halfspace, σ_{half} . Solid and dashed lines distinguish positive and negative values. The ratio between the halfspace conductivity and the target conductivity ($\sigma_\infty/\sigma_{half}$), is fixed to 10, whereas σ_{half} varies (10 $^{-4}$ –0.1 S/m). (b) Plots of the $|d^{IP}|/|d^F|$ ratio, R . In the grey region $R < 1$ and the strength of the IP signal is smaller than the EM signal. The legend for both plots is shown in (b).

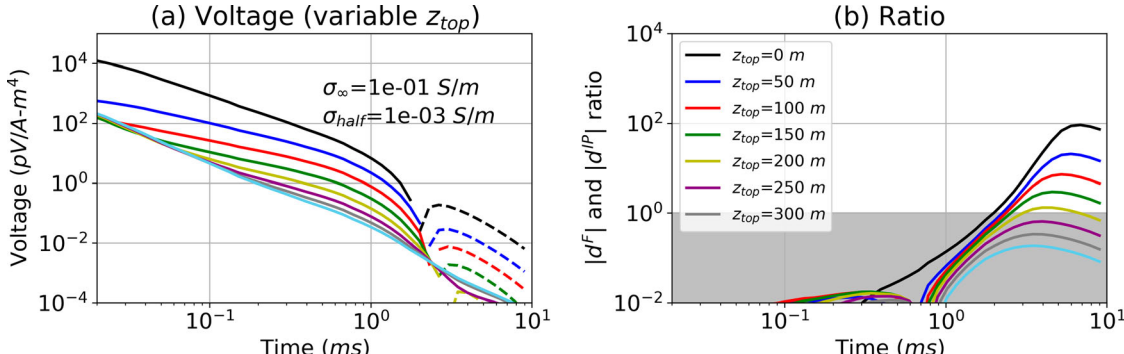


Figure 7. (a) Time decay curves with a variable target depth (z_{top}) ranging from 0 to 350 m. The halfspace conductivity is 10 $^{-3}$ S/m. (b) Plots of $R = |d^{IP}|/|d^F|$. In the grey region $R < 1$ and the strength of the IP signal is smaller than the EM signal. The legend for both plots is shown in (b).

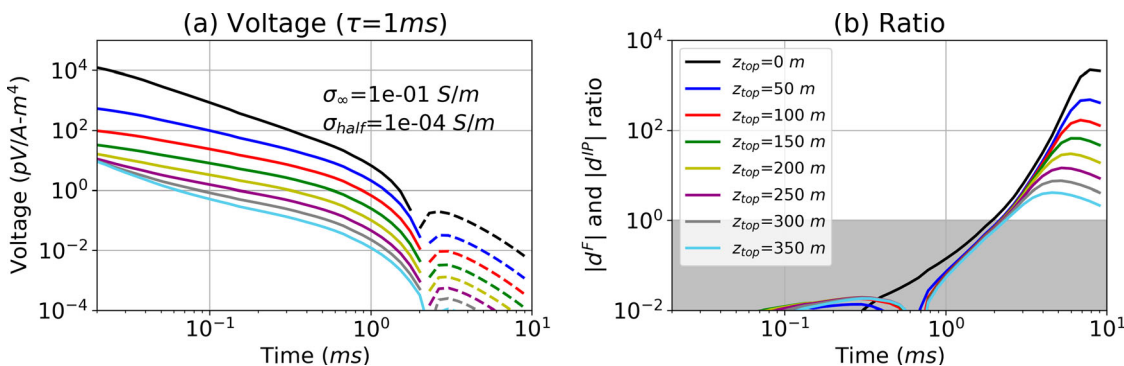


Figure 8. (a) Time decay curves with a variable target depth (z_{top}) ranging from 0–350 m. The halfspace conductivity is decreased to 10 $^{-4}$ S/m compared to Figure 7. (b) Plots of $R = |d^{IP}|/|d^F|$. In the grey region $R < 1$ and the strength of the IP signal is smaller than the EM signal. The legend for both plots is shown in (b).

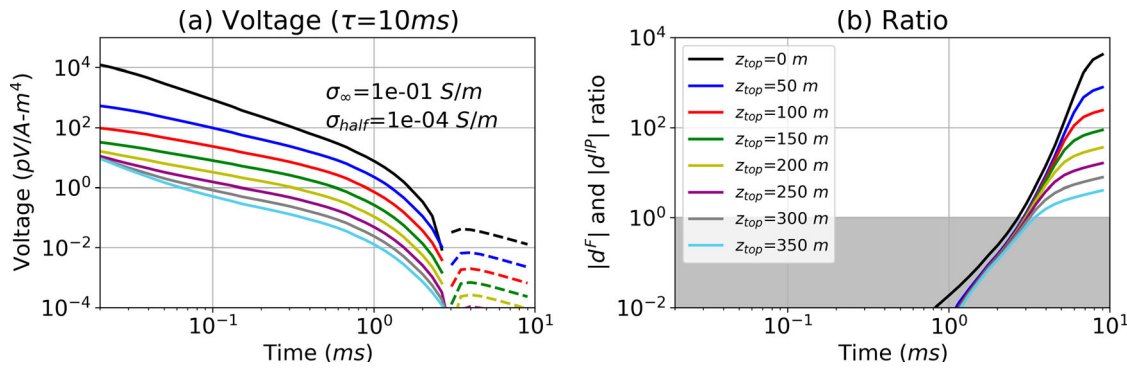


Figure 9. (a) Time decay curves with a variable target depth (z_{top}) ranging from 0–350 m. The time constant (τ) is increased to 10^{-2} s. (b) $|d^P|/|d^F|$ ratio, R . Grey region indicates $R < 1$ meaning the strength of the IP signal is smaller than EM signal.

in a resistive host rock (10^{-4} S/m); it was located ~ 70 m below the surface and its radius and thickness were approximately 150 m and 200 m, respectively (Kang, Fournier, and Oldenburg 2017). This geometry is similar to that of our chargeable cylinder shown in Figure 2.

The maximum depth that we can see negatives will depend upon IP parameters. For instance, greater chargeability will increase the strength of the IP signals and therefore the maximum depth can be increased with increased chargeability (Macnae 2016). The effects of the time constant are more complicated to unravel. We explore this by changing the time constant of the target from 1 ms to 10 ms and altering the depth of burial. We obtain Figure 9 and observe that the maximum depth is decreased from 350 m to 250 m. Performing a similar analyses for the time constant ranging from 0.1 ms to 10 s, we obtain the maximum depth as a function of the time constant as shown in Figure 10. The maximum depth starts from zero when $\tau_{se} = 0.1$ ms, increases until $\tau_{se} = 1$ ms, and then decreases as τ_{se} increases. We simulated two cases in which σ_{half} was 10^{-3} S/m and 10^{-4} S/m but the conductivity of the target (σ_∞) was fixed to 10^{-1} S/m. Greater maximum depth is shown when $\sigma_{half} = 10^{-4}$ S/m. Hence there is an optimal time constant (~ 1 ms) that can generate the greatest IP signals. This can be understood from the following. Considering the measured time range of the data: 10^{-2} – 10 ms, there simply not enough time to charge up material that has time constant greater than 3 s. Further, when the IP decay is too fast (small time constant) compared to EM decay, it is hard to be the signal in the observation.

3.3. The effects of target size

The examples shown so far have illustrated general principles concerned with the ability to detect IP bodies at depth. We have dealt with a specific geometry and have worked with a fairly large target. The strength of the IP signal depends upon the size and geometry of the target. To begin an exploration of the impact of target size on detectability, we show the effects of making

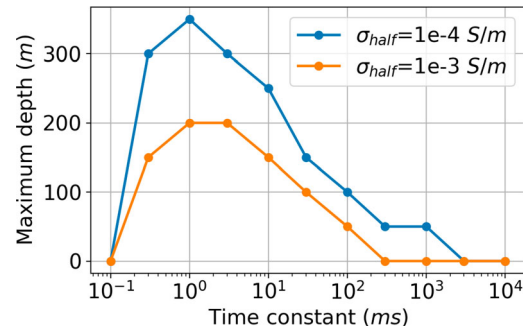


Figure 10. Maximum depth of the chargeable cylinder at which we can observe negative transients as a function of the time constant (ms). Light blue and orange lines indicate two conductivity models having different halfspace conductivity (σ_{half}): 10^{-4} S/m and 10^{-3} S/m, respectively.

the body smaller. We first reduce the radius (r) from 200 m to 50 m. As a result, the maximum depth has decreased from 300 m (Figure 8) to 100 m as shown in Figure 11. We can also reduce the thickness (h), as shown in Figure 12; here $z_{top} = 150$ m and $r = 100$ m. When $h = 10$ m, we no longer observe the negatives. Depending on the geological setting, more complicated situations may occur and the potential for seeing an IP signal in the airborne data will require 3D modelling appropriate to the geology. For instance, layering of the subsurface can also make significant impact to the maximum depth in practice, and this was not taken account in our analyses.

3.4. Which are the characteristics of detectable chargeable materials in AEM data?

The different polarisation characteristics of earth materials can be translated into different Cole-Cole or SE parameters. In particular, their frequency spectrum, or the time period over which the polarisation process is occurring, differs; this time period is closely related to the time constant, τ . For instance, fine-grained sulphides will show a higher frequency spectrum and smaller time constant than coarse-grained sulphides. Ground and airborne surveys such as DC-IP

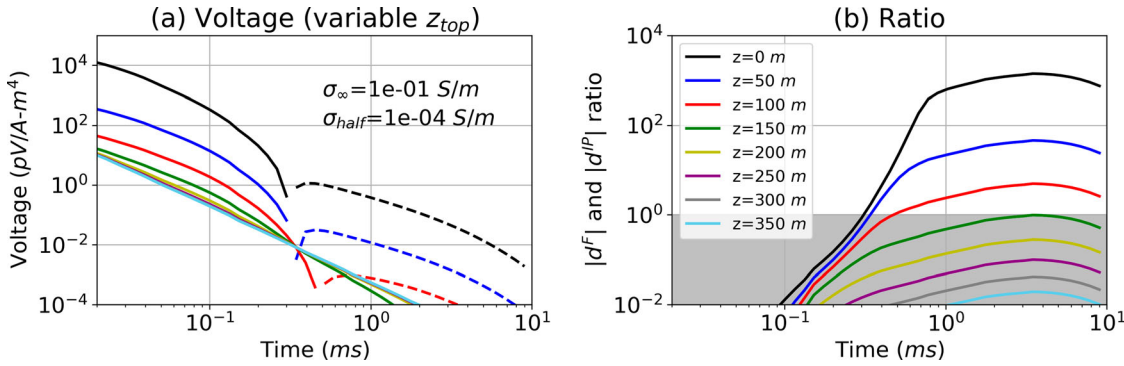


Figure 11. (a) Time decay curves with a variable target depth (z_{top}). The radius (r) of the chargeable cylinder is decreased from 200 m to 100 m compared to Figure 8. (b) $|d^IP|/|d^F|$ ratio, R . Grey region indicates $R < 1$ meaning the strength of the IP signal is smaller than EM signal.

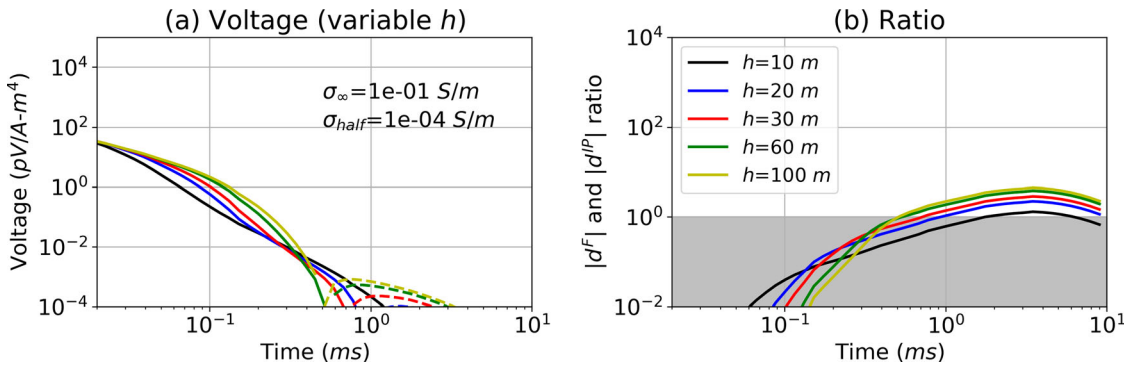


Figure 12. (a) Time decay curves with a variable target thickness (h). The radius (r) and depth to the top (z_{top}) of the chargeable cylinder are fixed to 50 m and 150 m, respectively, whereas h varies (10–100 m) as shown in the legend in (b) which displays the $|d^IP|/|d^F|$ ratio. Grey region indicates $R < 1$ meaning the strength of the IP signal is smaller than EM signal.

and AEM often use different base frequencies: e.g. 0.125 Hz and 25 Hz. As AEM surveys have a higher base frequency, they are more sensitive to chargeable materials which are characterised by high frequency or smaller time constants. Three main chargeable targets of interest in airborne IP are (a) fine-grained sulphides (Pelton et al. 1978; Revil et al. 2017), (b) clays (Leroy and Revil 2009; Macnae 2016), and (c) ice (Grimm and Stillman 2015; Kang, Fournier, and Oldenburg 2017). In Figure 13, we have plotted the frequency spectrum of each of these materials along with the frequency spectrum of DC-IP and AEM surveys.

To examine how each of these materials impacts the observed time decays, we have defined four models in Table 2 for which we will simulate AEM data. The decays, plotted in Figure 14, show the characteristic time behaviour associated each of the chargeable materials:

- Type A: Typical time decay showing positive early time data and negative late time data; this can be generated by fine-grained sulphides and clays.
- Type B: Double sign reversal; when sulphides or clays have very fine grain size the resulting time constant is smaller.

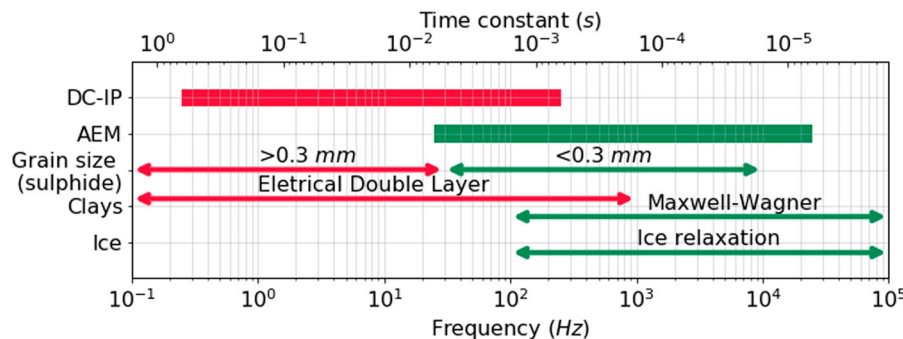


Figure 13. Frequency spectrum of EM systems (DC-IP and AEM) and various IP sources (sulphide, clays, and ice). The time constant is denoted at the top x-axis. This figure is based upon previous research (Grimm and Stillman 2015; Macnae and Hine 2016; Pelton et al. 1978; Revil 2013).

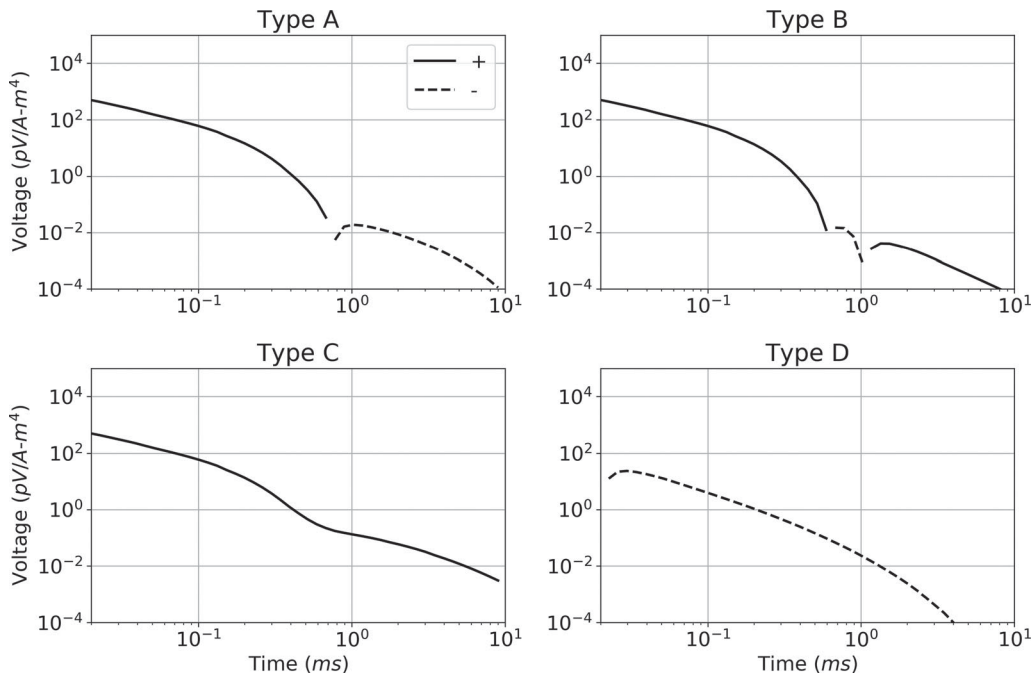


Figure 14. Four different types of time decays (A–D) from different sources of IP. Parameters used to compute time decays are summarised in Table 2.

Table 2. Parameters of the chargeable cylinder for the type curves (A–D) shown in Figure 9.

Division	Type A	Type B	Type C	Type D
Lithology	Clay Sulphide	Clay (finer) Sulphide (finer)	Type A with a deep conductor	Ice
z_{top} (m)	50	50	50	0
σ_{half} (S/m)	10^{-3}	10^{-4}	10^{-3}	10^{-4}
σ_∞ (S/m)	2×10^{-2}	2×10^{-2}	2×10^{-2}	10^{-3}
η_{se}	0.1	0.1	0.1	0.9
τ_{se} (ms)	1	0.1	1	0.08
c_{se}	0.7	0.7	0.7	0.5

Note: For Type C a conductive layer (0.1 S/m) is added 300 m below the surface; its thickness is 100 m.

- Type C: No negatives, but a positive “bump” at late time; this is when there is a deep conductor below a chargeable target, which can generate strong positive EM signals at late time.
- Type D: No positives; this can be generated by an extremely chargeable target such as ice ($\simeq 0.9$) located very near surface, or not measuring early enough time channels.

4. Conclusions

We have developed a convolutional TEM simulation code that directly solves Maxwell’s equations in time with the SE (stretched exponential) conductivity function. The SE conductivity is a good representation of the Cole-Cole conductivity for the typical time range used in AEM. With our simulations, we showed that:

- Negative transients in AEM data can be caused by the reversed direction of the electric field in a chargeable target and are visible at late times when EM induction is small.

- Moderately conductive targets (0.01–0.1 S/m) in a resistive host (10^{-4} – 10^{-3} S/m) show the best potential for generating strong IP signals (negatives) in AEM data.
- The depth at which we can detect a target with airborne IP depends upon the background conductivity, but for an ideal situation (a conductive, chargeable target in a resistive host), the target can be detected up to 300 m depth provided its time constant is close to 1 ms. This maximum depth will naturally be affected by the layering, but this was not taken account in our analyses.
- The strength of the IP signals and the depth of detectability of a target is dependent upon the size of the target and its geometry. In general 3D simulations, cast within the relevant geologic context, are required.
- The three main sources of chargeable material detectable in AEM (fine grain sulphides, clay and ice) can give rise to four different characteristic decay curves.

The overriding question of practical concern is whether, or under what circumstances, you can see an IP target at depth in airborne EM data. The situation is complex and cannot be answered by a simple, fixed depth of investigation rule. Forward simulation which emulates the potential geology and its associated physical properties, is required. To advance this capability, we have developed the SimPEG-EMIP codes as a part of the open-source software project, SimPEG (<https://www.simpeg.xyz>). The main workhorse for this paper has been the 2D cylindrical mesh, and the figures in this text can be reproduced with provided Jupyter

Notebooks (<https://github.com/simpeg-research/kang-2018-AEM>). Moreover, the source code is downloadable and users can explore the use of different parameters. We hope these efforts contribute to the wider challenge of extracting IP information from airborne time-domain EM data.

Disclosure statement

No potential conflict of interest was reported by the authors.

Funding

This work was funded by Mitacs.

ORCID

Seogi Kang  <http://orcid.org/0000-0002-9963-936X>
 Douglas W. Oldenburg  <http://orcid.org/0000-0002-4327-2124>
 Lindsey J. Heagy  <http://orcid.org/0000-0002-1551-5926>

References

- Belliveau P., and Haber E.. 2018. Coupled simulation of electromagnetic induction and induced polarization effects using stretched exponential relaxation. *Geophysics* 83: WB109–21.
- Cockett R., et al., 2015. SimPEG: an open source framework for simulation and gradient based parameter estimation in geophysical applications. *Computers and Geosciences* 85, no. Part A: 142–54.
- Cole K. S., and Cole R. H.. 1941. Dispersion and absorption in dielectrics I. Alternating current characteristics. *The Journal of Chemical Physics* 9: 341–51.
- Fink J., et al., 1990. *Induced polarization: Applications and case histories*. Vol. 4 of Society of Exploration Geophysicists. doi:[10.1190/1.9781560802594](https://doi.org/10.1190/1.9781560802594)
- Fitterman D. V., and Anderson W. L.. 1987. Effect of transmitter turn-off time on transient soundings. *Geoexploration* 24: 131–46.
- Grimm R. E., and Stillman D. E.. 2015. Field test of detection and characterization of subsurface ice using broadband spectral induced polarization. *Permafrost and Periglacial Process* 26: 28–38.
- Haber E. 2014. *Computational methods in geophysical electromagnetics*. SIAM.
- Heagy L. J., et al., 2017. A framework for simulation and inversion in electromagnetics. *Computers and Geosciences* 107: 1–19.
- Hodges G., and Chen T.. 2014. IP effect in airborne TDEM data: model studies and field examples. *SEG Technical Program Expanded Abstracts* 158: 828–32.
- Hyman J., et al., 2002. Mimetic finite difference methods for diffusion equations. *Computational Geosciences* 6: 333–52.
- Kaminski V., and Viezzoli A.. 2017. Modeling induced polarization effects in helicopter time-domain electromagnetic data: field case studies. *Geophysics* 82: B49–61.
- Kang S. 2018. On recovering distributed induced polarization information from time-domain electromagnetic data. PhD thesis, University of British Columbia.
- Kang S., Fournier D., and Oldenburg D.. 2017. Inversion of airborne geophysics over the DO-27/DO-18 kimberlites – part 3: induced polarization. *Interpretation* 5: T327–40.
- Kang S., and Oldenburg D. W.. 2017. TEM-IP: extracting more IP information from galvanic source time domain EM data. *Geophysical Prospecting* 6 (S1): 74–86.
- Kohlrausch R. 1854. Theorie des elektrischen rückstandes in der leidener flasche. *Annalen der Physik* 167: 179–214.
- Kratzer T., and Macnae J.. 2012. Induced polarization in airborne EM. *Geophysics* 77: E317–27.
- Kwan K., et al., 2015. Airborne inductive induced polarization chargeability mapping of VTEM data. *ASEG Extended Abstracts* 1–5.
- Leroy P., and Revil A.. 2009. A mechanistic model for the spectral induced polarization of clay materials. *Journal of Geophysical Research: Solid Earth* 114: 1–21.
- Macnae J. 2016. Quantifying airborne induced polarization effects in helicopter time domain electromagnetics. *Journal of Applied Geophysics* 135: 495–502.
- Macnae J., and Hine K.. 2016. Comparing induced polarization responses from airborne inductive and galvanic ground systems: tasmania. *Geophysics* 81: E471–79.
- Marchant D. 2015. Induced polarization effects in inductive source electromagnetic data. PhD thesis, University of British Columbia.
- Marchant D., Haber E., and Oldenburg D. W.. 2014. Three-dimensional modeling of IP effects in time-domain electromagnetic data. *Geophysics* 79: E303–14.
- Pelton W., et al., 1978. Mineral discriminatio and removal of inductive coupling with multifrequency IP. *Geophysics* 43: 588–609.
- Revil A. 2013. On charge accumulation in heterogeneous porous rocks under the influence of an external electric field. *Geophysics* 78(4): 1JA–Z103.
- Revil A., et al., 2017. Induced polarization response of porous media with metallic particles – part 6: the case of metals and semimetals. *Geophysics* 82: E97–110.
- Smith R. S., and Klein J. 1996. A special circumstance of airborne induced-polarization measurements. *Geophysics* 61: 66–73.
- Tarasov A., and Titov K. 2013. On the use of the Cole-Cole equations in spectral induced. *Polarization: i* 195: 352–6.
- Viezzoli A., Kaminski V., and Fiandaca G.. 2017. Modeling induced polarization effects in helicopter time domain electromagnetic data: synthetic case studies. *Geophysics* 82: E31–50.
- Weidelt P. 1982. Response characteristics of coincident loop transient electromagnetic systems. *Geophysics* 47: 1325–30.

Appendices

Appendix 1. Discretization

In this section, we discuss important elements about discretising Maxwell's equations in the time-domain with the convolution term shown in Equation (A9), to simulate IP effects in time-domain EM data. Appendix A.1 illustrates how convolutionary time-domain Maxwell's equations can be discretised. Appendix A.2 describes how the singularity of SE conductivity function at $t = 0$ is handled. Most of key challenges about this discretization are tackled in Marchant (2015) (see page 21), and we have extended his work, applied for Cole-Cole conductivity, to SE conductivity.

A.1 Maxwell's equations

The stretched exponential (SE) conductivity provided in Equation (8) in the time-domain can be rewritten as

$$\sigma_{se}(t) = \sigma_{\infty}\delta(t) + \Delta\sigma(t), \quad (A1)$$

where $\delta(t)$ is a Dirac-Delta function and $\Delta\sigma(t)$ is

$$\Delta\sigma(t) = -\sigma_\infty \eta_{se} t^{-1} \left(\frac{t}{\tau_{se}} \right)^{c_{se}} \exp\left(-\left(\frac{t}{\tau_{se}}\right)^{c_{se}}\right) \quad (\text{A2})$$

Considering a time-dependent conductivity, Ohm's Law can be written as

$$\vec{j} = \sigma_{se}(t) \otimes \vec{e} = \int_0^t \sigma(t-u) \vec{e}(u) du \quad (\text{A3})$$

and substituting Equation (A1) yields

$$\vec{j} = \sigma_\infty \vec{e} + \int_0^t \Delta\sigma(t-u) \vec{e}(u) du \quad (\text{A4})$$

Using the Backward Euler method, we discretise Maxwell's equations in Equations (4) and (5) in time:

$$\vec{\nabla} \times \vec{e}^{(n)} = -\frac{\vec{b}^{(n)} - \vec{b}^{(n-1)}}{\Delta t^{(n)}} \quad (\text{A5})$$

$$\vec{\nabla} \times \mu^{-1} \vec{b}^{(n)} - \vec{j}^{(n)} = \vec{j}_s^{(n)}, \quad (\text{A6})$$

where $\Delta t^{(n)} = t^{(n)} - t^{(n-1)}$. To discretise the integral in Equation (A4), we use the trapezoidal rule:

$$\begin{aligned} \int_{t^{(k-1)}}^{t^{(k)}} \Delta\sigma(t-u) \vec{e}(u) du &= \frac{\Delta t^{(k)}}{2} \left(\Delta\sigma(t^{(n)}) - t^{(k-1)} \right) \vec{e}^{(k-1)} \\ &\quad + \Delta\sigma(t^{(n)} - t^{(k)}) \vec{e}^{(k)} \end{aligned} \quad (\text{A7})$$

Figure A1 shows a conceptual diagram for this discrete convolution procedure. Hence Equation (A4) can be discretised as

$$\begin{aligned} \vec{j}^{(n)} &= \sigma_\infty \vec{e}^{(n)} + \sum_{k=1}^n \frac{\Delta t^{(k)}}{2} \left(\Delta\sigma(t^{(n)}) - t^{(k-1)} \right) \vec{e}^{(k-1)} \\ &\quad + \Delta\sigma(t^{(n)} - t^{(k)}) \vec{e}^{(k)} \end{aligned} \quad (\text{A8})$$

This can be rewritten as

$$\vec{j}^{(n)} = \left(\sigma_\infty + \gamma(\Delta t^{(n)}) \right) \vec{e}^{(n)} + \vec{j}_{pol}^{(n-1)}, \quad (\text{A9})$$

where the polarization current, $\vec{j}_{pol}^{(n-1)}$ is

$$\begin{aligned} \vec{j}_{pol}^{(n-1)} &= \sum_{k=1}^{n-1} \frac{\Delta t^{(k)}}{2} \left(\Delta\sigma(t^{(n)}) - t^{(k-1)} \right) \vec{e}^{(k-1)} \\ &\quad + \Delta\sigma(t^{(n)} - t^{(k)}) \vec{e}^{(k)} + \kappa(\Delta t^{(n)}) \vec{e}^{(n-1)} \end{aligned} \quad (\text{A10})$$

For the simplest case when ($c_{se} = 1$), then $\Delta\sigma(t=0)$ is well-defined and $\gamma(\Delta t^{(n)})$ and $\kappa(\Delta t^{(n)})$ are respectively:

$$\gamma(\Delta t^{(n)}) = \frac{\Delta t^{(n)}}{2} \Delta\sigma(0), \quad (\text{A11})$$

$$\kappa(\Delta t^{(n)}) = \frac{\Delta t^{(n)}}{2} \Delta\sigma(\Delta t^{(n)}) \quad (\text{A12})$$

However, when $c_{se} \neq 1$, $\Delta\sigma(t=0)$ is singular and hence it requires special numerical treatment; this is described in Appendix A.2.

For the discretization, we use a staggered mimetic finite volume approach (Hyman et al. 2002). Here, boldface with uppercase and lowercase indicate matrices and column vectors, respectively. Further details about the discretization can be found in Haber (2014) (see page 31). Discretising Equations (A5), (A6), and (A9) yields

$$\mathbf{C}\mathbf{e}^{(n)} = -\frac{\mathbf{b}^{(n)} - \mathbf{b}^{(n-1)}}{\Delta t^{(n)}} \quad (\text{A13})$$

$$\mathbf{C}\mathbf{M}_{\mu^{-1}}^f \mathbf{b}^{(n)} - \mathbf{M}^e \mathbf{j}^{(n)} = \mathbf{s}_e^{(n)}, \quad (\text{A14})$$

$$\mathbf{M}^e \mathbf{j}^{(n)} = \mathbf{M}_A^e \mathbf{e}^{(n)} + \mathbf{j}_{pol}^{(n-1)}, \quad (\text{A15})$$

where

$$\begin{aligned} \mathbf{j}_{pol}^{(n-1)} &= \sum_{k=1}^{n-1} \frac{\Delta t^{(k)}}{2} \left(\mathbf{M}_{\Delta\sigma(n,k-1)}^e \vec{e}^{(k-1)} + \mathbf{M}_{\Delta\sigma(n,k)}^e \mathbf{e}^{(k)} \right) \\ &\quad + \mathbf{M}_k^e \mathbf{e}^{(n-1)} \end{aligned} \quad (\text{A16})$$

Here, \mathbf{C} is the discrete edge-curl operator; \mathbf{M}^e and \mathbf{M}^f are the edge and face inner-product matrices, respectively. For an inner-product matrix, the subscript indicates corresponding physical property (e.g. $M_{\mu^{-1}}^f$: the face inner-product matrix for μ^{-1}).

Rearranging the above equations to solve for \mathbf{e} yields:

$$\begin{aligned} \left(\mathbf{C}^T \mathbf{M}_{\mu^{-1}}^f \mathbf{C} + \frac{1}{\Delta t^{(n)}} \mathbf{M}_A^e \right) \mathbf{e}^{(n)} &= -\frac{1}{\Delta t^{(n)}} (\mathbf{s}_e^{(n)} - \mathbf{s}_e^{(n-1)}) \\ &\quad + \frac{1}{\Delta t^{(n)}} \mathbf{M}^e \mathbf{j}^{(n-1)} - \frac{1}{\Delta t^{(n)}} \mathbf{j}_{pol}^{(n-1)} \end{aligned} \quad (\text{A17})$$

By solving the above equation at each time step, we obtain \mathbf{e} . The measured data for AEM are often $-db/dt$, which can be computed as

$$\mathbf{d}/\mathbf{dt} = -\mathbf{C}\mathbf{e} \quad (\text{A18})$$

The measured data at a receiver loop can be expressed as

$$\mathbf{d} = \mathbf{P}(-\mathbf{d}/\mathbf{dt}), \quad (\text{A19})$$

where \mathbf{P} is an interpolation matrix, which projects \mathbf{d}/\mathbf{dt} fields, defined in a 3D domain, to a receiver location, and samples those fields at the measured time channels. For discretisation of Equations (A17) to (A19) we use, SIMPEG's mesh toolbox. The developed code is open-source as a SIMPEG-EMIP package (<https://github.com/sgkang/simpegEMIP>)

A.2 Handling the singularity at $\sigma(t = 0)$

The SE conductivity, $\sigma_{se}(t)$ at $t = 0$, is singular, whereas its integral is well-defined, as shown in Equation (6). When discretising Equation (A3), this singularity will be problematic. In particular, the issue occurs at the last time segment ($k = n$) of the convolution term in Equation (A8), which can be written in continuous form:

$$\int_{t^{n-1}}^{t^n} \Delta\sigma(u) \vec{e}(t-u) du \quad (\text{A20})$$

This problem also occurs when the Cole-Cole function is used. Marchant (2015) (see page 31) tackled this issue by approximating \vec{e} at this time segment as a linear function:

$$\begin{aligned} \vec{e}(t) &= \frac{t^n - t}{\Delta t^{(n)}} \vec{e}^{(n-1)} + \frac{t - t^{n-1}}{\Delta t^{(n)}} \vec{e}^{(n-1)}, \\ \text{when } (t^{n-1}) &\leq t \leq t^n \end{aligned} \quad (\text{A21})$$

Then by substituting this in to Equation (A20), and evaluating the integration, the discrete form of Equation (A20) is obtained:

$$\int_{t^{n-1}}^{t^n} \Delta\sigma(u) \vec{e}(t-u) du \simeq \kappa(\Delta t^{(n)}) \vec{e}^{(n-1)} + \gamma(\Delta t^{(n)}) \vec{e}^{(n)} \quad (\text{A22})$$

To obtain $\gamma(\Delta t^{(n)})$ and $\kappa(\Delta t^{(n)})$, we use the same trick. Integration of $\Delta\sigma(t)$ is not possible, so by Taylor expanding, we obtain an approximate form of $\Delta\sigma(t)$ which is valid for small t :

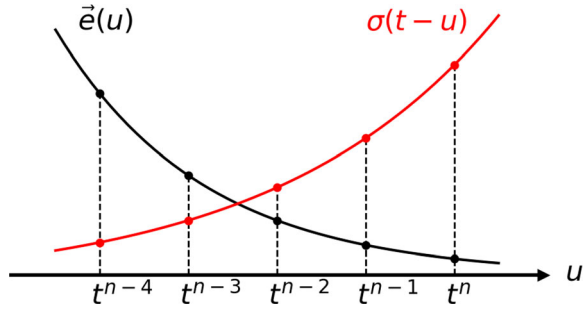


Figure A1. Conceptual diagram to describe discrete convolution process in Equation (A7)

$$\begin{aligned}\Delta\sigma(t) &= -\sigma_\infty \eta_{se} t^{-1} \left(\frac{t}{\tau_{se}}\right)^{c_{se}} \exp\left(-\left(\frac{t}{\tau_{se}}\right)^{c_{se}}\right) \\ &\approx -\sigma_\infty \eta_{se} t^{-1} \left(\frac{t}{\tau_{se}}\right)^{c_{se}} \left(1 - \left(\frac{t}{\tau_{se}}\right)^{c_{se}}\right) \\ &= -\sigma_\infty \eta_{se} t^{-1} \left(\left(\frac{t}{\tau_{se}}\right)^{c_{se}} - \left(\frac{t}{\tau_{se}}\right)^{2c_{se}}\right)\end{aligned}\quad (\text{A23})$$

By substituting Equation (A23) into Equation (A20) and evaluating the integral, we finally obtain

$$\gamma(\Delta t^{(n)}) = \sigma_\infty m \left(\frac{(\Delta t^{(n)})^{c_{se}}}{c_{se}(c_{se} + 1)} - \frac{(\Delta t^{(n)})^{2c_{se}}}{2c_{se}(2c_{se} + 1)\tau_{se}^{c_{se}}} \right) \quad (\text{A24})$$

$$\kappa(\Delta t^{(n)}) = \sigma_\infty m \left(\frac{(\Delta t^{(n)})^{c_{se}}}{c_{se} + 1} - \frac{(\Delta t^{(n)})^{2c_{se}}}{(2c_{se} + 1)\tau_{se}^{c_{se}}} \right) \quad (\text{A25})$$

Appendix 2. Analytic test

To test the developed SIMPEG-EMIP code, we compare our numerical solution with an analytic solution. A halfspace earth

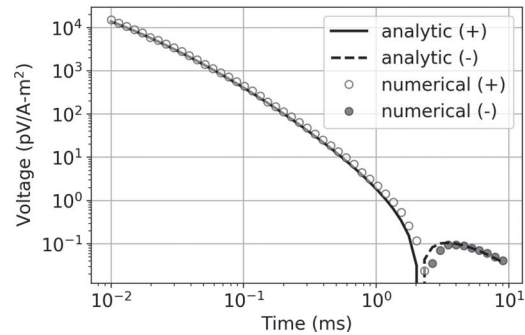


Figure A2. Comparison of numerical and analytic solutions for halfspace earth. SE parameters of the halfspace earth are $\sigma_\infty = 0.05 \text{ S/m}$, $\eta_{se} = 0.7$, $\tau_{se} = 4 \text{ ms}$, $c_{se} = 0.6$; corresponding Cole-Cole parameters are: $\eta_{cc} = 0.8$, $\tau_{cc} = 5 \text{ ms}$, $c_{cc} = 0.6$. Lines and circles distinguish analytic and numerical solutions.

is assumed. The conductivity of the halfspace is 0.05 S/m and its SE parameters are: $\eta_{se} = 0.7$, $\tau_{se} = 4 \text{ ms}$, $c_{se} = 0.6$. Corresponding Cole-Cole parameters are: $\eta_{cc} = 0.8$, $\tau_{cc} = 0.005 \text{ s}$, $c_{cc} = 0.6$. For the spatial discretization, a 2D cylindrically symmetric mesh is used; the smallest cell size is $6.5 \text{ m} \times 5 \text{ m}$. A horizontal source loop is located 30 m above the surface. A step-off waveform is used for the input current and a horizontal receiver loop measuring the voltage (equivalent to $-db_z/dt$) is coincident with the source loop. Data are measured in the off-time over the time-range: 10^{-2} – 10 ms . Figure A2 shows comparison between analytic and numerical solutions; they match well except for a small shift in the time of the zero-crossing, the two solutions are in good agreement.